Stability and Bifurcation Analysis of DC Microgrid With Multiple Droop Control Sources and Loads

Haiyuan Liu, Wenzhong Guo, Dong Cheng, Yingjie Wang, *Member, IEEE*, and Min Wang

***Abstract*—With the increasing of dc microgrid scale and complexity, it is urgent to obtain the stability rules of dc microgrid. In this article, the dc microgrid model with multiple droop control sources and loads is first established for its inner diversity. By analyzing the distribution of eigenvalues, static characteristics and bifurcation, the key factors and critical conditions of stability and bifurcation of the dc microgrid system are obtained, and the quantitative relationship between the system stability and the parameters such as droop coefficient, line impedance, dc bus capacitance, and load is determined. Additionally, the guidance is provided for the stability judgment of dc microgrid. Finally, the effectiveness of the conclusions is verified by the real-time hardware-in-loop experiments.**

***Index Terms*—Bifurcation, dc microgrid, droop control, stability.**

NOMENCLATURE

C_i	Capacitance of the ith dc bus capacitor.
i	Current or number.
i_{dc}	Output current of DCS.
i_{ref}	Given current of internal controller of CPS.
j	Imaginary unit or number.
k	Droop coefficient.
n, m	Number.
P_{s}	Power delivered of CPS.
P_{L}	Power absorbed of CPL.
P_{CPS}	Total power of CPSs.
P_{CPL}	Total power of CPLs.
R_{load}	Tesistance of active load.
R_i	Resistance of the ith resistive load.
u	Voltage.
u_{dc}	Output voltage of DCS.
u_{dc}^*	Given voltage of internal controller of DCS.
u_{load}	Output voltage of active load.
U_{ref}	Given voltage of droop control of DCS.
σ	Real part of eigenvalue λ.
ω	Imaginary part of eigenvalue λ.

I. INTRODUCTION

WITH the increasing attention to the reliability and power quality [1], [2], as well as the large-scale application of distributed generations (DGs), microgrid as an attractive choice of distributed power access to the grid has been widely concerned [3], [4]. Compared with ac microgrid, dc microgrid has the highlight advantages of high efficiency, low cost, simple control, and high reliability [5]. Moreover, reactive power and skin effect issues are absent from dc microgrid. At present, it has been successfully applied in many specific occasions [6], such as residential building, car charging system, mine power supply, etc.

In dc microgrid with droop control, each droop control source (DCS) autonomously participates in dc-bus voltage control, and the communication is not vital [7]. Hence, this dc microgrid is relatively more reliable and easier to achieve "plug-and-play." However, droop control changes output characteristics of sources, and a virtual resistance [8] is equivalently added to make them farther away from an ideal source. Additionally, constant power loads (CPLs) tend to decrease damping of dc microgrid [9]–[11]. These cause a great interaction between sources and loads interfere with dc-bus voltage and even lead to its instability. A lot of research has been carried out to explore the stability of dc microgrid.

The stability analysis of dc microgrid mainly focuses on small-signal stability at present, including small-signal modeling and small signal analysis. In [12]–[14], the detailed and accurate state-space model and the impedance-based criterion widely used in this stability analysis is established by Middlebrook and Cuk. Based on it, some researches have successfully addressed the instability of CPLs around the voltage operating point of dc microgrid [15]–[17].

Although the state-space model is accurate for expressing the internal control of each converter, the system model of it will become complex with the increase of converters. Therefore, some scholars have been attempting to the simplification of the dc microgrid model. In [18], the singular perturbations technique is utilized to obtain reduced-order models of islanded microgrid at different time-scales. In [19], the converter is equivalent to voltage source, current source or constant power source (CPS)

Manuscript received January 8, 2020; revised May 3, 2020; accepted June 28, 2020. Date of publication July 14, 2020; date of current version September 22, 2020. This work was supported in part by the National Key R&D Program of China under Grant 2016YFC0600906 and in part by the Xuzhou Promoting Science and Technology Innovation Projects under Grant KC18076. Recommended for publication by Associate Editor J. M. Guerrero. *(Corresponding author: Yingjie Wang.)*

Haiyuan Liu is with the School of Mathematics, China University of Mining and Technology, Xuzhou 221116, China (e-mail: liu6340@126.com).

Wenzhong Guo, Yingjie Wang, and Min Wang are with the School of Electrical and Power Engineering, China University of Mining and Technology, Xuzhou 221116, China (e-mail: gwz94666@163.com; wyj971@126.com; 1126648731@qq.com).

Dong Cheng is with the CSIC 713th Research Institute, Zhengzhou 450000, China (e-mail: 411822234@qq.com).

This article has supplementary downloadable material available at https://ieeexplore.ieee.org, provided by the authors.

Color versions of one or more of the figures in this article are available online at https://ieeexplore.ieee.org.

Digital Object Identifier 10.1109/TPEL.2020.3009192

according to their working characteristics, and the two-order model of the dc microgrid is obtained, which leads to some sufficient conditions for the stable operation being deduced for the first time. However, in practical systems, it is not easy to satisfy its hypothesis that the ratio of the droop coefficient of each DG to the corresponding line inductance is equal.

Small-signal stability analysis methods generally include impedance-based criterion and eigenvalue analysis methods. In [20], based on the gain margin and phase margin criterion, the stability of the hybrid energy storage system investigated provides the requirements for the parameter design of the proposed control strategy. In [21], considering the robustness of stability, the proposed maximum peak criterion can ensure that the system has a certain stability margin. There are additional, such as the opposing argument criterion [22], energy source analysis consortium criterion [23], root exponential stability criterion [24], etc. The earlier criteria for setting different stability margins and forbidden zones are all based on the impedance. In [25], the eigenvalue analysis method is used to derive the conditions that the droop coefficient should be satisfied during stable operation of the system, and the sensitivity of system poles to variation in cable impedance is also performed. In [26], for dc microgrid with multiple dc electric springs, the eigenvalue analysis is presented to investigate the effect of the communication weight on system stability. These methods and conclusions are suitable for local stability analysis near to the voltage operating point. However, the DCSs are allowed to work on voltage along droop curves, making the linear analysis on the special operating point unsuitable for stability analysis for the entire range of possible voltages. So it is difficult to obtain the stability rules that are the main concern during the design of dc microgrid.

In this article, first, the simplified model of dc microgrid system is established. The real parts of the eigenvalues of the Jacobian matrix are analyzed rather than calculating the specific eigenvalues for the stability rules. By analyzing the distribution of eigenvalues, static characteristics and bifurcation [27], [28], the stability boundary and instability behavior mechanism of the system are obtained. Then, based on these analysis conclusions, the effect of system parameters, such as resistive load, CPL, droop coefficient, dc-bus capacitance, transmission line impedance, is discussed on the dc microgrid stability. And the stability judgment guidance is also designed. Finally, the hardware-in-loop (HIL) real-time simulation experiments verify the correctness and validity of the conclusions proposed in this article.

II. MODELING OF DC MICROGRID

A dc microgrid with multiple types of DCSs and loads is shown in Fig. 1. It mainly consists of DCSs, CPSs, CPLs, dc-bus capacitors, resistive loads, and distribution cables. The modeling in this article is based on the following assumptions.

1) Intermittent sources with maximum power point tracking (MPPT) (such as photovoltaic and wind power), considered as CPS, and Loads are in a local loading area. The distribution cables connecting with them can be equivalent to an ideal wire due to the close distance.
2) DGs, considered as DCSs, in distributed power plants come from relatively remote areas, and the impedances on the transmission lines cannot be ignored.
3) All the converters in the dc microgrid always keep working normally and track the control instructions quickly.

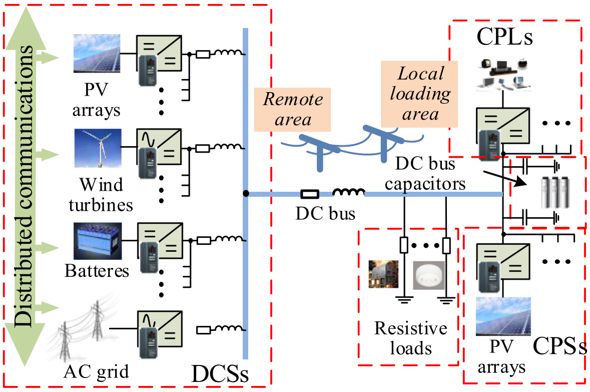

Fig. 1. DC microgrid with multiple DCSs and loads.

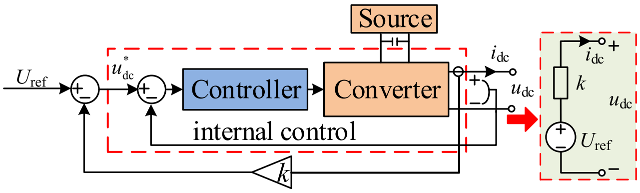

Fig. 2. Control structure of DCS.

A. Droop Control Source

It is assumed that that the structure of all DCSs is same, as shown in Fig. 2. U_{ref} and k can be different due to the different capacity and distribution position of the DCSs. Compared with the response of dc microgrid system, the internal control process of DCS takes up little time, which can be considered as instantaneous completion. The DCS can be equivalent to a voltage source U_{ref} and a virtual droop resistance k in series, as illustrated in Fig. 2.

In a distributed power plant, it can be assumed that there may be n DCSs of the same type that have the same capacity and control mode. DCSs in different distributed power plants require different droop curves to achieve reasonable load sharing. Considering the impedance on the transmission line, the equivalent model of DCSs is shown in Fig. 3. Here, k_{11}/n_1 is considered to be k_1 in the latter article. In the right figure of Fig. 3, equivalent impedance can be obtained as

$$R_{\mathrm{d}i} = k_i + R_{\mathrm{L}i} + R_{\mathrm{L}} \frac{1}{i_{\mathrm{dc}i}} \sum_{j=1}^{n} i_{\mathrm{dc}j}, \quad i = 1, 2, \cdots, n \tag{1}$$

$$L_{\mathrm{d}i} = L_{\mathrm{L}i} + L_{\mathrm{L}} \frac{1}{\mathrm{d}i_{\mathrm{dc}i}} \mathrm{d}\left(\sum_{j=1}^{n} i_{\mathrm{dc}j} \right), \quad i = 1, 2, \cdots, n \tag{2}$$

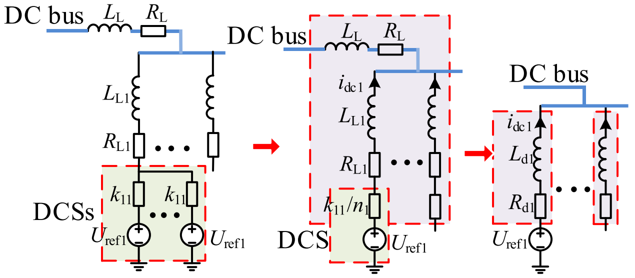

Fig. 3. Equivalent circuit of n type of DCSs.

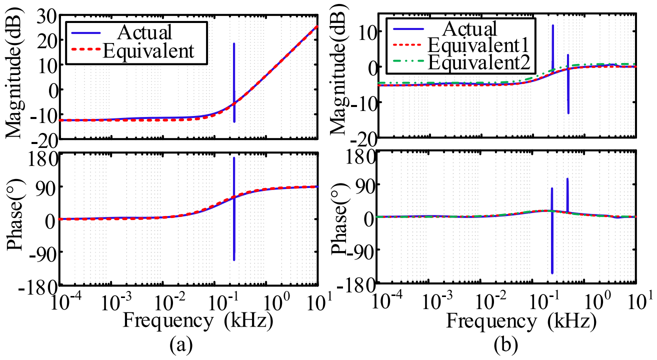

(a) (b)

Fig. 4. Bode diagram of the impedance. (a) Impedances of DCS. (b) Impedance ratios.

where $i_{\mathrm{dc}i}$ and $i_{\mathrm{dc}j}$ are the output current of DCS #*i* and DCS #*j*, respectively. $R_{\mathrm{L}i}$ and $L_{\mathrm{L}i}$ are the impedances on the transmission line between DCS #*i* with the dc bus. R_{L} and L_{L} are DC bus impedance. $R_{\mathrm{d}i}$ and $L_{\mathrm{d}i}$ are the equivalent impedance. k_i is the droop coefficient of DCS #*i*.

According to (1) and (2), these equivalent impedances are time-varying. When *n* DCSs are connected in parallel, the distribution proportions of the output currents are mainly determined by the droop coefficients of themselves, if the transmission line is short or the condition $k_i/k_j \approx R_{\mathrm{L}i}/R_{\mathrm{L}j} \approx L_{\mathrm{L}i}/L_{\mathrm{L}j}$ is met. So the following assumption is made

$$\frac{1}{i_{\mathrm{dc}i}}\sum_{j=1}^{n} i_{\mathrm{dc}j} \approx \frac{1}{\mathrm{d}i_{\mathrm{dc}i}}\mathrm{d}\left(\sum_{j=1}^{n} i_{\mathrm{dc}j}\right) \approx k_i \sum_{j=1}^{n}\frac{1}{k_j}. \tag{3}$$

Substituting (3) into (1) and (2), these equivalent impedances can be approximated as the constants

$$R_{\mathrm{d}i} \approx k_i + R_{\mathrm{L}i} + R_{\mathrm{L}}k_i \sum_{i=1}^{n}\frac{1}{k_i}, \quad i = 1, 2, \cdots, n \tag{4}$$

$$L_{\mathrm{d}i} \approx L_{\mathrm{L}i} + L_{\mathrm{L}}k_i \sum_{i=1}^{n}\frac{1}{k_i}, \quad i = 1, 2, \cdots, n. \tag{5}$$

Refer to the experimental parameters later, Bode diagram of the impedance is drawn in Fig. 4. Fig. 4(a) shows the actual impedance and the equivalent impedance of DCS #1 branch. Fig. 4(b) shows the impedance ratios of DCS #1 branch to DCS #2 branch, including in the actual impedance ratio without bus impedance, the equivalent impedance ratio without bus impedance (equivalent 1) and the equivalent impedance ratio with bus impedance (equivalent 2). From Fig. 4(a), the curves of the actual impedance and the equivalent impedance almost coincide, which shows that the equivalence of DCS is reasonable. From Fig. 4(b), the impedance ratio curves of the three models have little difference, which shows that the approximate condition in (3) is reasonable and effective.

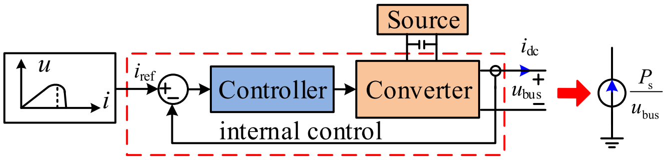

Fig. 5. Control structure of the intermittent sources with MPPT.

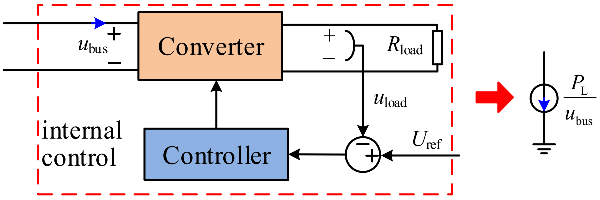

Fig. 6. Control structure of the active load.

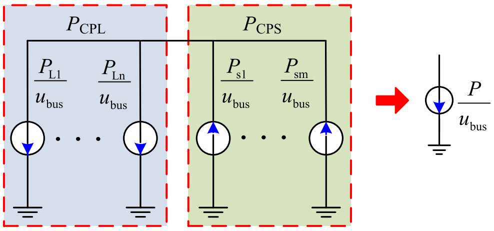

Fig. 7. Equivalent model of CPSs and CPLs.

B. Constant Power Source and Constant Power Load

The intermittent sources with MPPT keep the maximum power output as soon as possible. The active loads usually keep the load side voltage constant. As long as the load resistance is constant, the power absorbed is constant. If the loss is ignored, the power absorbed or delivered will not change when the dc-bus voltage fluctuates within the design range. Similarly, the internal control process can be considered as instantaneous completion relative to response time of dc microgrid. So, it is generally considered that intermittent source with MPPT and active load can be equivalent to CPS and CPL, respectively, as illustrated in Figs. 5 and 6. In a local area, the same type of CPS or CPL can be combined with each other, as illustrated in Fig. 7

$$P = \sum_{i=1}^{n} P_{\mathrm{L}i} - \sum_{i=1}^{m} P_{\mathrm{S}i} \tag{6}$$

where P is the total power of CPSs and CPLs, $P_{\mathrm{L}i}$ is the power absorbed of CPL #*i*, and $P_{\mathrm{S}i}$ is the power delivered of CPS #*i*.

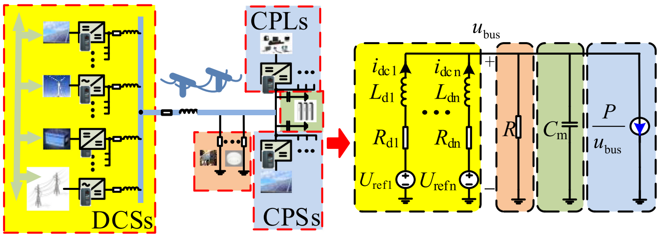

Fig. 8. Equivalent circuit model of dc microgrid.

C. Equivalent Circuit Model of DC Microgrid

In a local loading area, dc-bus capacitors and resistive loads are connected to an ideal wire, and can be equivalent

$$C_m=\sum_{i=1}^{n}C_i,\quad R=\frac{1}{\sum_{i=1}^{n}1/R_i}\tag{7}$$

where C_{m} is the total capacitance of the dc-bus capacitors, and R is the total resistance of the resistive loads.

Combining the above equivalence, an equivalent circuit model of dc microgrid is established, as shown in Fig. 8. There are n DCSs, a dc-bus capacitance C_{m}, a resistance R and a CPL in this model.

Based on this equivalent circuit, the circuit equation of dc microgrid can be represented

$$\begin{cases}\frac{\mathrm{d}i_{\text{dc}i}}{\mathrm{d}t}=\frac{1}{L_{\text{d}i}}\left(-R_{\text{d}i}i_{\text{dc}i}+U_{\text{ref}i}-u_{\text{bus}}\right),i=1,2,\cdots,n\\ \frac{\mathrm{d}u_{\text{bus}}}{\mathrm{d}t}=\frac{1}{C_m}\left(i_{\text{dc1}}+\cdots+i_{\text{dc}n}-\frac{u_{\text{bus}}}{R}-\frac{P}{u_{\text{bus}}}\right)\end{cases}\tag{8}$$

where the subscript i represents DCS #i, $U_{\text{ref}i}$ is the supply voltage of DCS #i, and u_{bus} is the voltage of dc bus.

III. STABILITY ANALYSIS OF DC MICROGRID

A. Eigenvalue Analysis of DC Microgrid

In this article, eigenvalue analysis method is used to analyze the stability rules of dc microgrid. From (8), the Jacobian matrix J of the system can be obtained as

$$J=\begin{bmatrix}-\frac{R_{d1}}{L_{d1}} & 0 & 0 & 0 & 0 & -\frac{1}{L_{d1}}\\ \vdots & \ddots & \vdots & \vdots & \vdots & -\frac{1}{L_{d2}}\\ 0 & \cdots & -\frac{R_{di}}{L_{di}} & \cdots & 0 & -\frac{1}{L_{di}}\\ \vdots & \vdots & \vdots & \ddots & \vdots & \vdots\\ 0 & \cdots & 0 & \cdots & -\frac{R_{dn}}{L_{dn}} & -\frac{1}{L_{dn}}\\ \frac{1}{C_m} & \cdots & \frac{1}{C_m} & \cdots & \frac{1}{C_m} & -\frac{1}{C_m}\left(\frac{1}{R}-\frac{P}{U_{\text{bus}}^2}\right)\end{bmatrix}\tag{9}$$

where U_{bus} is dc-bus voltage when the system is stable.

The system characteristic equation is as follows:

$$\frac{1}{C_m}\sum_{j=1}^{n}\left[\frac{1}{L_{dj}}\prod_{i=1,i\neq j}^{n}\left(\lambda+\frac{R_{di}}{L_{di}}\right)\right]+\left(\lambda+\frac{1}{RC_m}-\frac{P}{C_mU_{\text{bus}}^2}\right)\prod_{i=1}^{n}\left(\lambda+\frac{R_{di}}{L_{di}}\right)=0\tag{10}$$

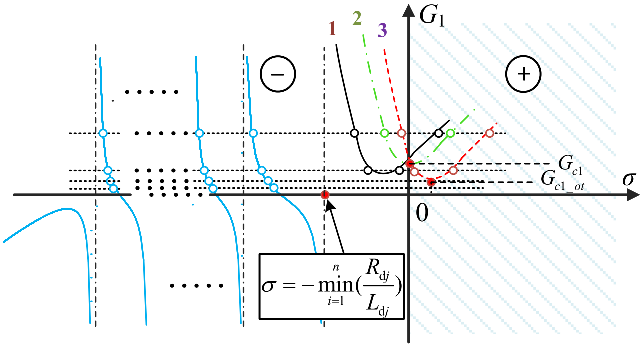

Fig. 9. Relationship diagram between G and σ under condition I.

where λ is the eigenvalue of the equation. Under the specific parameters, the $n+1$ eigenvalues of the system can be easily obtained, and the stability of the system can be judged by the eigenvalues, but it is difficult to find the relationships between the system parameters and the stability, through which the stability rules of dc microgrid are obtained furthermore. In this article, these relationships will be revealed by the real part of these eigenvalues. Set $\lambda=\sigma+j\omega$ and $G=P/U^2{}_{\text{bus}}$, and substitute them into (10)

$$\begin{cases}G=\sum_{j=1}^{n}\frac{\sigma+R_{dj}/L_{dj}}{L_{dj}\left[(\sigma+R_{dj}/L_{dj})^2+\omega^2\right]}+\sigma C_m+\frac{1}{R}\\ 0=\sum_{j=1}^{n}\frac{-\omega}{L_{dj}\left[(\sigma+R_{dj}/L_{dj})^2+\omega^2\right]}+\omega C_m.\end{cases}\tag{11}$$

The obtaining process of (11) is given in Appendix A. According to the second formula of (11), these eigenvalues meet one of the following two conditions.

Condition I:

$$\omega=0\tag{12}$$

or

Condition II:

$$\sum_{j=1}^{n}\frac{1}{L_{dj}\left[(\sigma+R_{dj}/L_{dj})^2+\omega^2\right]}=C_m.\tag{13}$$

Condition I:

These eigenvalues meeting condition I are all real eigenvalues. Substitute (12) into the first formula of (11)

$$G_1=\sum_{j=1}^{n}\frac{1}{L_{dj}\sigma+R_{dj}}+\sigma C_m+\frac{1}{R}\tag{14}$$

According to (14), the relationship diagram of G_1 and σ can be drawn, as illustrated in Fig. 9. According to whether the two largest real eigenvalues are greater than zero, there are three situations. At this time, the critical points are given in Table I. The three situations of Fig. 9 and Table I are detailed in Appendix B

$$G_{c1}=\sum_{j=1}^{n}\frac{1}{R_{dj}}+\frac{1}{R}\tag{15}$$

TABLE I
CRITICAL POINTS OF SYSTEMS UNDER DIFFERENT SITUATIONS

SITUATION	SYSTEM PARAMETERS	CRITICAL POINTS
(1)	$C_{\mathrm{m}} > \sum_{j=1}^{n} L_{\mathrm{d}j} / R_{\mathrm{d}j}^{2}$	$G_{\mathrm{c1}}(G_{\mathrm{c1}} > G_{\mathrm{cm}})$
(2)	$C_{\mathrm{m}} = \sum_{j=1}^{n} L_{\mathrm{d}j} / R_{\mathrm{d}j}^{2}$	$G_{\mathrm{c1}}(G_{\mathrm{c1}} = G_{\mathrm{c1\_ot}} > G_{\mathrm{cm}})$
(3)	$C_{\mathrm{m}} < \sum_{j=1}^{n} L_{\mathrm{d}j} / R_{\mathrm{d}j}^{2}$	$G_{\mathrm{c1\_ot}}(G_{\mathrm{c1}} > G_{\mathrm{cm}})$

$$G_{c1\_\mathrm{ot}} = \sum_{j=1}^{n} \frac{1}{L_{dj}\sigma_0 + R_{dj}} + \sigma_0 C_m + \frac{1}{R} < G_{c1} \tag{16}$$

$$G_{cm} = C_m \cdot \min_{j=1}^{n} (R_{dj}/L_{dj}) + \frac{1}{R} \tag{17}$$

where G_{c1} is the *G* corresponding to $\sigma = 0$, G_{c1_ot} is the minimum value on curve 1, 2 and 3, and σ_0 is the real eigenvalue corresponding to the minimum value G_{c1_ot}. G_{c1_ot} is uncertain because it contains an unknown real part of the eigenvalue. But, G_{c1_ot} is bigger than G_{cm} under situation (3). It can be concluded from Fig. 9: when $G \geq G_{c1\_\mathrm{ot}}$, the $n + 1$ eigenvalues of the system are all real eigenvalues. When $0 \leq G < G_{c1\_\mathrm{ot}}$, there are the *n*-1 real eigenvalues. And the remaining two eigenvalues satisfy condition II, which are conjugate complex eigenvalues.

Condition II:

Take the derivative of *G*, and substitute (13) into the first formula of (11).

$$\frac{\mathrm{d}G}{\mathrm{d}\sigma} = \sum_{j=1}^{n} \frac{2\omega^2}{L_{dj}\left[(\sigma + R_{dj}/L_{dj})^2 + \omega^2\right]^2} > 0. \tag{18}$$

It can be seen that the relationship between σ and *G* is monotonously increasing. When $\sigma = 0$, substituting (13) into the first formula of (11), the critical point $G_{\mathrm{c}2}$ of the system appears

$$G_{c2} = \sum_{j=1}^{n} \frac{R_{dj}/L_{dj}}{L_{dj}\left[(R_{dj}/L_{dj})^2 + \omega^2\right]} + \frac{1}{R} < G_{c1}. \tag{19}$$

$G_{\mathrm{c}2}$ is also indeterminate for there is the imaginary part. But, $G_{\mathrm{c}2}$ is similarly bigger than G_{cm}.

Although the critical points (G_{c1}, G_{c1_ot}, and G_{c2}) have been found, the stability rules of the system will be given by combining the later static characteristic analysis and bifurcation analysis.

B. Static Characteristic Analysis

The purpose of static characteristic analysis is to obtain the stable equilibrium points of the system. When the derivative of the state variables in state equation is zero, the stable equilibrium points of the system can be calculated. The two equilibrium points, $p_i = [I_{1i}, \cdots, I_{ni}, U_{\mathrm{bus}i}]$, $i = 1, 2$, are obtained by setting the differential terms of (8) to zero

$$\begin{cases} p_1 = \left(\frac{U_{\mathrm{ref}1} - U_{\mathrm{bus}1}}{R_{d1}}, \ldots, \frac{U_{\mathrm{ref}n} - U_{\mathrm{bus}1}}{R_{dn}}, \right. \\ \qquad \left. \frac{\sum_{j=1}^{n} \frac{U_{\mathrm{ref}j}}{R_{dj}} - \sqrt{\left(\sum_{j=1}^{n} \frac{U_{\mathrm{ref}j}}{R_{dj}}\right)^2 - 4P\left(\sum_{j=1}^{n} \frac{1}{R_{dj}} + \frac{1}{R}\right)}}{2\left(\sum_{j=1}^{n} \frac{1}{R_{dj}} + \frac{1}{R}\right)} \right) \\ p_2 = \left(\frac{U_{\mathrm{ref}1} - U_{\mathrm{bus}2}}{R_{d1}}, \ldots, \frac{U_{\mathrm{ref}n} - U_{\mathrm{bus}2}}{R_{dn}}, \right. \\ \qquad \left. \frac{\sum_{j=1}^{n} \frac{U_{\mathrm{ref}j}}{R_{dj}} + \sqrt{\left(\sum_{j=1}^{n} \frac{U_{\mathrm{ref}j}}{R_{dj}}\right)^2 - 4P\left(\sum_{j=1}^{n} \frac{1}{R_{dj}} + \frac{1}{R}\right)}}{2\left(\sum_{j=1}^{n} \frac{1}{R_{dj}} + \frac{1}{R}\right)} \right). \end{cases} \tag{20}$$

From (20), the necessary condition for the existence of equilibrium points is

$$P < P_{\max} = \left(\sum_{j=1}^{n} \frac{U_{\mathrm{ref}j}}{R_{dj}}\right)^2 \bigg/ 4\left(\sum_{j=1}^{n} \frac{1}{R_{dj}} + \frac{1}{R}\right). \tag{21}$$

The another expression of *G* can be obtained by setting the differential terms of (8) to zero

$$G = \sum_{j=1}^{n} \frac{U_{\mathrm{ref}j}/U_{\mathrm{bus}} - 1}{R_{dj}} - \frac{1}{R}. \tag{22}$$

Then substituting (15) into (22), the relationship between *P* and *G* at the equilibrium points is obtained

$$P = \left(\sum_{j=1}^{n} \frac{U_{\mathrm{ref}j}}{R_{dj}}\right)^2 \frac{G}{(G + G_{c1})^2} \tag{23}$$

According to (22), substitute G_{c1} and G_{cm}, respectively, and obtain the corresponding power P_{c1} and P_{cm}

$$\begin{cases} P_{c1} = P_{\max} = \left(\sum_{j=1}^{n} \frac{U_{\mathrm{ref}j}}{R_{dj}}\right)^2 \Big/ 4\left(\sum_{j=1}^{n} \frac{1}{R_{dj}} + \frac{1}{R}\right) \\ Pcm = \left(\sum_{j=1}^{n} \frac{U_{\mathrm{ref}j}}{R_{dj}}\right)^2 \frac{G_{cm}}{(G_{c1} + G_{cm})^2}. \end{cases} \tag{24}$$

Then, also from (19) and (20), the *G* values corresponding to equilibrium points are obtained, as shown in (25). From (25), it is obvious that G_{p1} is greater than G_{c1} and G_{p2} is smaller than G_{c1}.Under the same parameters, the position of static equilibrium point is not unique. There are two equilibrium points and the corresponding *G* values, which also reflect the nonlinearity. However, there is only one stable static equilibrium point, which will be further explained in the next

$$\begin{cases} G_{p1} = G_{c1}\left(\frac{2}{1 - \sqrt{1 - P/P_{\max}}} - 1\right) \\ G_{p2} = G_{c1}\left(\frac{2}{1 + \sqrt{1 - P/P_{\max}}} - 1\right) \end{cases} \tag{25}$$

where G_{p1} and G_{p2} represent the *G* at equilibrium points p_1 and p_2, respectively.

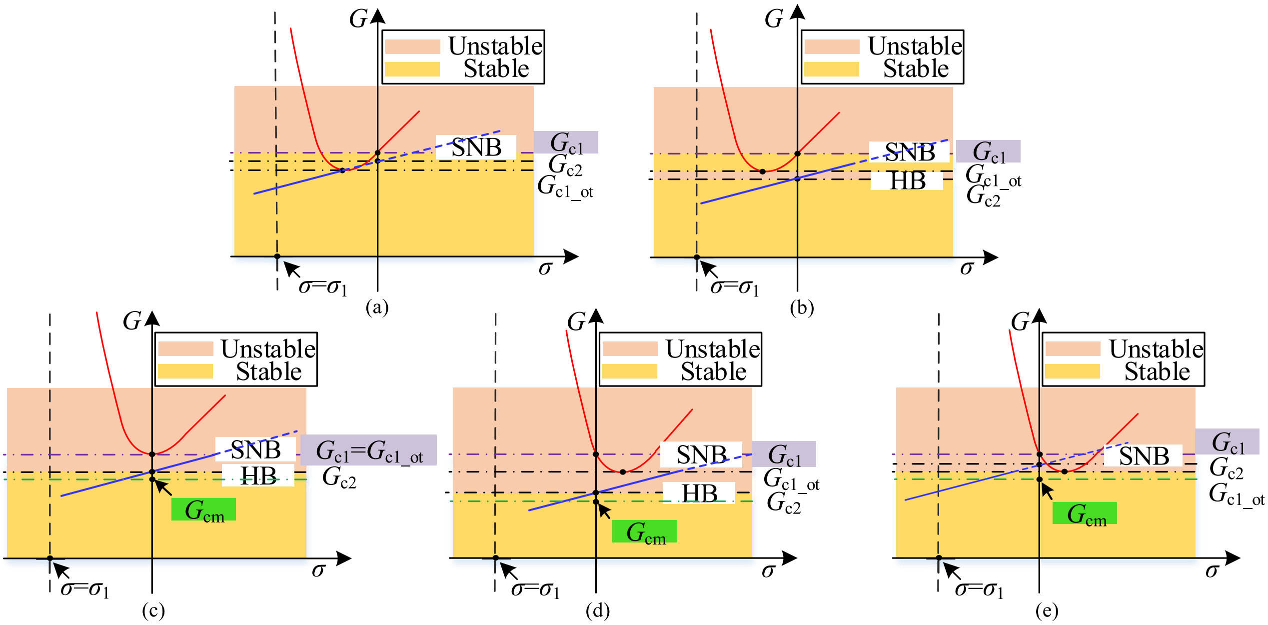

Fig. 10. Stability and bifurcation of the system. (a) Situation (1) and $G_{c2} \geq G_{c1\_ot}$. (b) Situation (1) and $G_{c2} < G_{c1\_ot}$. (c) Situation (2). (d) Situation (3) and $G_{c2} < G_{c1\_ot}$. (e) Situation (3) and $G_{c2} \geq G_{c1\_ot}$.

C. Bifurcation Analysis and Conclusions

Bifurcation analysis is usually used to analyze the instability behavior. In this article, the small signal stability based on linearized model is studied, and its corresponding bifurcation type is local bifurcation. The global bifurcation is based on the nonlinear model, so the global bifurcation is not considered. Local bifurcations mainly include saddle-node bifurcation (SNB) and Hopf bifurcation (HB).

When SNB occurs, the Jacobian matrix is singular, which there is no equilibrium point and the dc-bus voltage collapses. The determinant of the system Jacobian matrix is formulated as

$$|J| = (-1)^{\mathrm{n}} \left(G - G_{\mathrm{c}1}\right) \prod_{j=1}^{n} R_{dj}/L_{dj}. \tag{26}$$

When $G = G_{c1}$, the Jacobian matrix is singular matrix. SNB occurs.

When HB occurs, there is a pair of conjugate eigenvalues at the imaginary axis. At this time, the system will bifurcate from the equilibrium point to the limit cycle and produce periodic oscillation. When condition II exists, there is a pair of conjugate eigenvalues. When the conjugate eigenvalues are in the virtual axis, HB will occur.

In summary, if $G > G_{c1\_ot}$, the all eigenvalues λ satisfy the condition I, that is, the λ are all real eigenvalues. System stability is only determined by condition I. With the increasing of G, SNB occurs when $G = G_{c1}$. If $0<G<G_{c1\_ot}$, the eigenvalues have n-1 real eigenvalues and two imaginary eigenvalues. System stability is determined by conditions I and II. If $G_{c2}<G_{c1\_ot}$, HB occurs when $G = G_{c2}$.

Combined with eigenvalue analysis, Fig. 10 shows five stability and bifurcation situations of the system. Red line represents the relationship between G and σ of the two largest real eigenvalues under condition I, which refers to Fig. 9. Blue line represents the relationship between G and σ of the two conjugate eigenvalues under condition II, which refers to (17). Blue dotted line represents no conjugate eigenvalue because all the eigenvalues are real at $G > G_{c1\_ot}$.

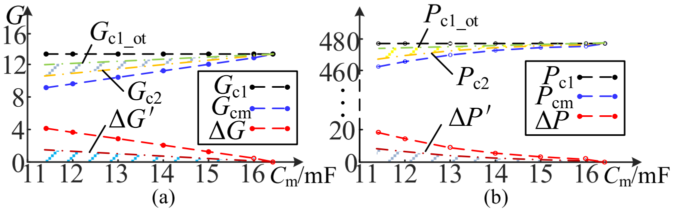

Fig. 11. HB region under situation (1). (a) G_{c1}, G_{cm}, and ΔG. (b) P_{c1}, P_{cm}, and ΔP.

In Fig. 10(a), there are SNB at $G = G_{c1}$ and the system goes through "stable state ($G < G_{c1}$) → SNB ($G = G_{c1}$) → unstable state ($G > G_{c1}$)." In Fig. 10(b), with the increase of G, the system goes through "stable state ($G < G_{c2}$) → HB ($G_{c2} \leq G < G_{c1\_ot}$) → stable state ($G_{c1\_ot} \leq G < G_{c1}$) → SNB ($G = G_{c1}$) → unstable state ($G > G_{c1}$)." As illustrated in Fig. 11, under situation (1) and $G_{c2} < G_{c1\_ot}$, with the increase of C_m, G_{c1}, and G_{cm} are gradually approaching. According to the following experimental parameters, their maximum difference value of ΔP ($P_{c1} = 478$ kW, $P_{cm} = 461$ kW) is 17 kW, which is enough small to be submerged by power fluctuation. Also because of $G_{c2} > G_{cm}$ and $G_{c1\_ot} < G_{c1}$, in Fig. 10(b) the HB region is small enough to be neglected. Therefore, it can be considered that the system goes through "stable state ($G < G_{c1}$) → SNB ($G = G_{c1}$) → unstable state ($G > G_{c1}$)." So, in Fig. 10(a) and (b), the stable region of the system is $G < G_{c1}$.

TABLE II
STABILITY AND BIFURCATION OF DC MICROGRID SYSTEM

CASE	DC bus capacitance	stability region	Bifurcation point	Figure
A	$C_{\mathrm{m}} > \sum_{j=1}^{n} L_{\mathrm{d}j} / R_{\mathrm{d}j}^2$	$G<G_{\mathrm{c1}}$	G=G_{c1}, SNB	Fig.10 (*a*)
		$G<G_{\mathrm{c1}}$ (Approximately)	G=G_{c2}, HB (Neglected); G=G_{c1}, SNB	Fig.10 (*b*)
B	$C_{\mathrm{m}} \le \sum_{j=1}^{n} L_{\mathrm{d}j} / R_{\mathrm{d}j}^2$	$G<G_{\mathrm{cm}}$	G=G_{c2}, HB; G=G_{c1}, SNB	Fig.10 (*c*), (*d*)
			G=G_{c1}, SNB	Fig.10 (*e*)

TABLE III
SYSTEM PARAMETERS OF DC MICROGRID

Description	Value	Description	Value
Input voltage V_{in1}, V_{in5}	200V	DC bus capacitance C_{m}	1mF
Input voltage V_{in2}	100V	Droop coefficient k_1	0.2
Input voltage V_{in3}	160V	Droop coefficient k_2, ..., k_5	0.4
Input voltage V_{in4}	180V	Resistance load R	50Ω
Line resistance $R_{\mathrm{L}i}$	0.04Ω	Output voltage of CPL u_{load}	200V
Line inductance $L_{\mathrm{L}i}$	0.3mH	Switching frequency f_{s}	20kHz

In Fig. 10(c) and (d), the system goes through "stable state ($G < G_{c2}$) → HB ($G_{c2} \le G < G_{c1}$) → SNB ($G = G_{c1}$) → unstable state ($G > G_{c1}$)." In Fig. 8(e), there are no two conjugate eigenvalues at $G = G_{c2}$, and the system goes through "stable state ($G < G_{c1\_\mathrm{ot}}$) → unstable state ($G_{c1\_\mathrm{ot}} \le G < G_{c1}$) → SNB ($G = G_{c1}$) → unstable state ($G > G_{c1}$)." G_{c1_ot} and G_{c2} cannot be calculated because they contain unknown eigenvalues, but G_{c1_ot} is bigger than G_{cm} under situation (3), and G_{c2} is bigger than G_{cm}. So, in Fig. 10(c)–(e), it can be considered that the stable region of the system is $G < G_{cm}$.

To sum up the above analysis, the stability and bifurcation of dc microgrid can be given in Table II, which is divided into two cases.

For the equilibrium point p_1, the corresponding G_{p1} is greater than G_{c1}, and no matter in case A or case B, all p_1 points are unstable equilibrium points. For the equilibrium point p_2, the corresponding G_{p2} is smaller than G_{c1}, so all p_2 points are stable equilibrium points in case A. In case B, only p_2 points with $G_{p2} < G_{cm}$ are stable equilibrium points, and the system at p_2 points with $G_{cm} \le G_{p2} < G_{c1}$ is unstable, which probably generates unstable limit cycle of HB. The stability and bifurcation of the equilibrium point p_1 and p_2 is shown in Fig. 12. The difference between the HB and SNB bifurcation points calculated by simulation and the theoretical points are small when the resistance R increases.

IV. FACTORS AFFECTING THE STABILITY OF DC MICROGRID

A. *Influence of System Parameters on Stability*

Fig. 13 shows the relationship between system parameters and P_{c1} *or* P_{cm} that is respectively the corresponding power of G_{c1} and G_{cm}. System parameters refer to Table III. k_1 represents droop coefficient of the DCS #1 on R_{d1}/L_{d1} of which has the minimum value; L_{d1} represents equivalent line inductance of the DCS #1; and k_2 represents droop coefficient of the DCS #2.

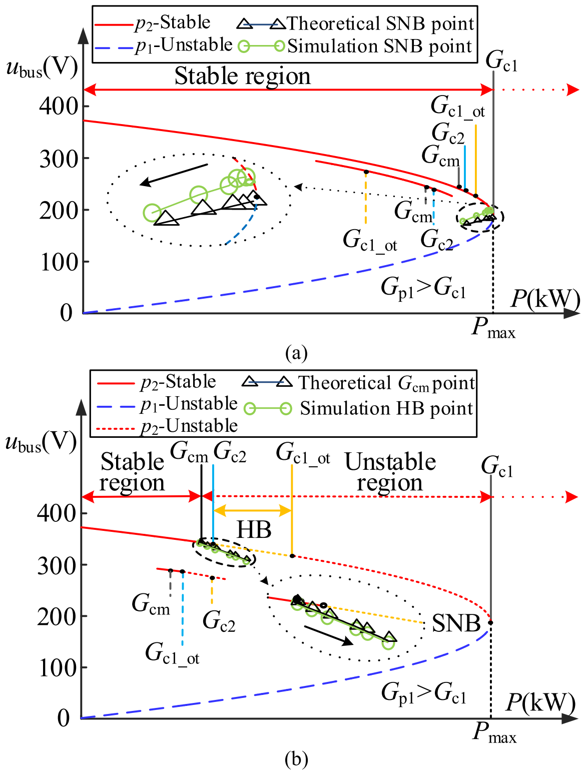

(a)

(b)

Fig. 12. Stability and bifurcation of equilibrium point p_1 and p_2. (a) Case A. (b) Case B.

P_{c1} is independent of C_m from (23). So in case A, only reducing droop coefficient k or increasing R will improve P_{c1}, shown in Fig. 13(a) and (b).

In case B, increasing C_m will improve P_{cm}, shown in Fig. 13(c). Fig. 13(d) shows that P_{cm} decreases with increasing of R no matter how C_m changes. But, when R reaches a certain value, P_{cm} almost remains unchanged. Moreover, with increasing of C_m, the influence of R on system stability decreases. In Fig. 13(e), the increase of L_{d1} will reduce P_{cm} no matter how C_m changes. In Fig. 13(f), with increasing of k_1, P_{cm} increases first. When $k_1 = k_2$, P_{cm} is the largest, and continuing to increase k_1, P_{cm} is almost unchanged. The reason is that when $k_1 > k_2$, R_{d1}/L_{d1} will be no longer the minimum value, and P_{cm} will be determined by R_{d2}/L_{d2}.

B. *Stability Judgment Guidance of the DC Microgrid*

DC-bus voltage varies with current in droop control and G varies accordingly. But according to (21), the G is the largest at the minimum dc-bus voltage. Hence, the stability of dc microgrid can be determined by the stability of the system at the lower boundary point on droop curves. Ignoring the loss, P can be considered as output power of all the DCSs minus the power absorbed by the resistive loads, then the G is as follows:

$$G_{\max} = \left(\sum_{i=1}^{n} U_{d\mathrm{cmin}} I_{\mathrm{min}i} - U_{d\mathrm{cmin}}^2 / R \right) \Bigg/ U_{d\mathrm{cmin}}^2 \tag{27}$$

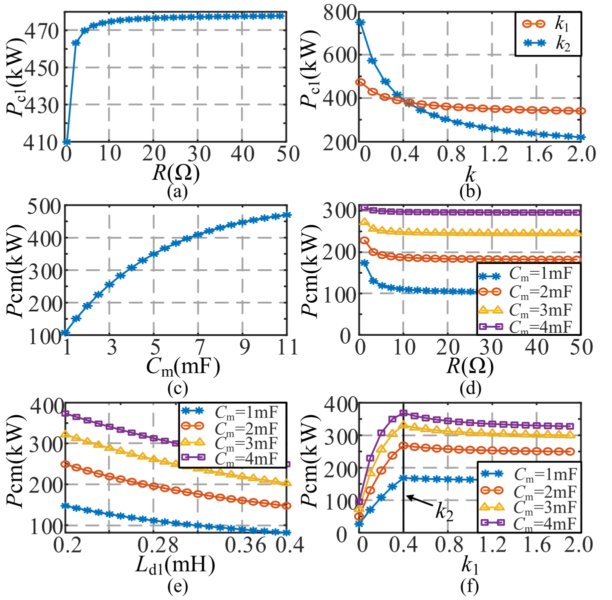

Fig. 13. Relationship between system parameters and P_{c1} or P_{cm}. (a) R and P_{c1}. (b) k and P_{c1}. (c) C_m and P_{cm}. (d) R and P_{cm}. (e) L_{dj} and P_{cm}. (f) k_1 and P_{cm}.

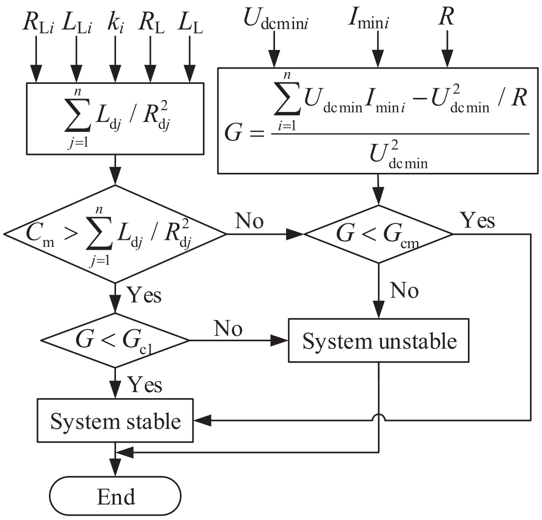

Fig. 14. Stability judgment guidance of the dc microgrid.

where U_{dcmin} is the lower boundary voltage on droop curves; $I_{\min i}$ is the current of the DCS #i corresponding to the lower boundary voltage on droop curves.

Based on the above conclusions, the stability judgment guidance of the dc microgrid is given, as shown in Fig. 14. This judgment guidance only needs to perform several unequal logic judgments, and it is not necessary to calculate the eigenvalues of the Jacobian matrix, which will greatly simplify stability judgment and design of dc microgrid.

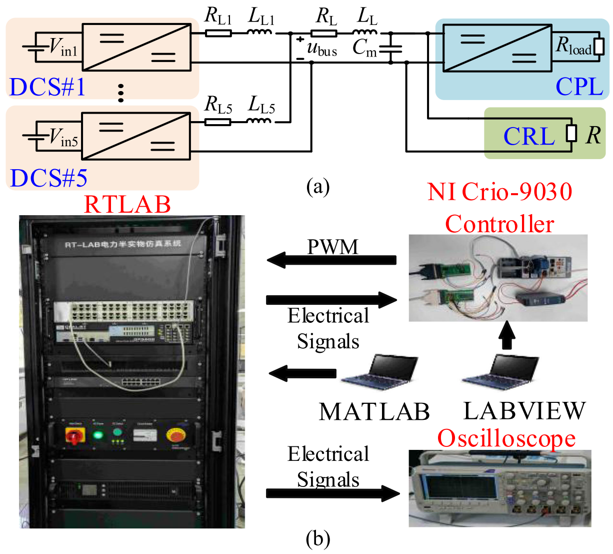

Fig. 15. Experimental system. (a) Experimental dc microgrid structure diagram. (b) HIL tests setup.

TABLE IV
CRITICAL G AND P IN DIFFERENT SITUZTIONS

CASE	status	Parameter	Critical G	Critical P
CASE A	I	R=1Ω, C_m=12mF	G_{c1}=14.26	P_{c1}=445kW
	II	R: 1Ω→50Ω	G_{c1}=13.26	P_{c1}=478kW
	III	k_2, …, k_5:0.4→0.3	G_{c1}=16.93	P_{c1}=541kW
CASE B	IV	C_m=1mF, R=50Ω	G_{cm}=0.82	P_{cm}=104.7kW
	V	C_m:1mF→1.5mF	G_{cm}=1.22	P_{cm}=147.0kW
	VI	R: 50Ω→2.5Ω	G_{cm}=1.2	P_{cm}=137.9kW
	VII	L_{d1}:0.3mH→0.2mH	G_{cm}=1.22	P_{cm}=147.0kW
	VIII	k_1:0.2→0.4	G_{cm}=1.22	P_{cm}=167.6kW
	IX	k_2, …, k_5:0.4→0.2	G_{cm}=0.82	P_{cm}=108.5kW

V. EXPERIMENTAL RESULT

To verify the conclusion of stability analysis about dc microgrid in this article, a dc microgrid model with five DCSs, one CRL and one CPL is carried out in Fig. 15. All the DCSs are boost converters with droop control and the CPL is Buck converter (380–150 V). The HIL tests are conducted using the RT-LAB and NI Crio-9030 controller. The equipment of the HIL tests is shown in Fig. 15(b).

Meanwhile, to verify the extreme situations, no upper and lower limit is set for voltage and current of the droop control in the dc microgrid. From the above analysis, the different reference voltages are only related to the static balance point and not to the stability region, which has no effect on the analysis conclusion verification. Therefore, all the $U_{\mathrm{ref}i}$ are set to 380 V, and other parameters of the system are given in Table III. According to the system parameters in Table III, $P_{\max} = 477.8$ kW, $\sum_{j=1}^{n} L_{dj}/R_{dj}^2 = 11.41$.

C. Case A

DC-bus capacitance is set to $C_m = 12$ mF that meet case A. $R = 1$ Ω, and the other parameters in Table III are unchanged. The stability of the dc microgrid must satisfy $G < G_{c1} = 14.26$, and the critical power P_{c1} is about 445 kW, as is shown in status (I) in Table IV. The dc-bus voltage waveform is shown in Fig. 16(a). At t_1, the power of CPL jumps up $P = 375$ kW $< P_{c1}$, the system is stable; at t_2, P jumps up $P = 450$ kW $> P_{c1}$, SNB occurs. According to the theoretical analysis, there

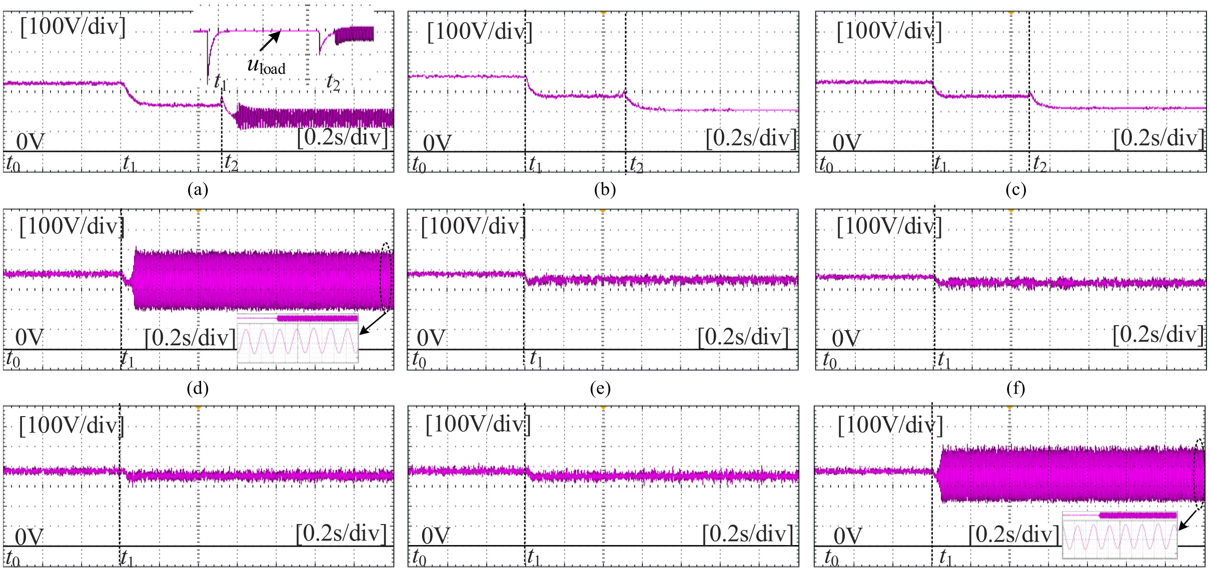

(a) (b) (c) (d) (e) (f) (g) (h) (i)

Fig. 16. DC-bus voltage waveforms corresponding to Table IV. (a) Status (I). (b) Status (II). (c) Status (III). (d) Status (IV). (e) Status (V). (f) Status (VI). (g) Status (VII). (h) Status (VIII). (i) Status (IX).

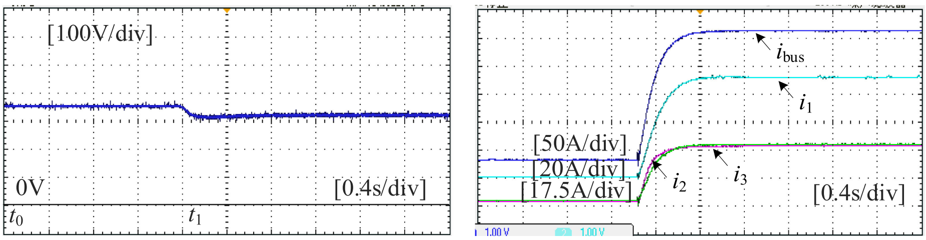

Fig. 17. Waveforms when bus impedance changes.

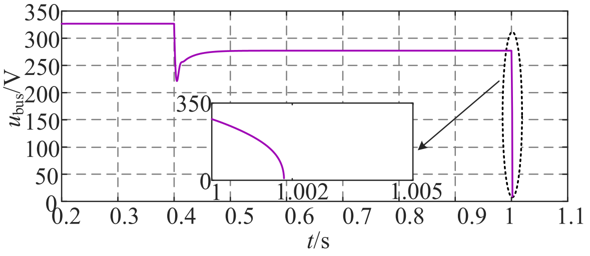

Fig. 18. Waveform of dc-bus voltage as a controlled current source being connected.

is no equilibrium point, and the dc-bus voltage drops sharply. However, during the experiment, the dc-bus voltage oscillates because the CPL converter is unstable and its output voltage oscillates. As shown in Fig. 18, when the controllable current source is used to simulate the CPL, the dc-bus voltage drops instantly at t_2, and the experimental process is automatically terminated, which is consistent with the theoretical analysis.

When the parameters change according to status (II) and (III)in Table IV, the dc-bus voltage waveforms are shown in Fig. 16(b) and (c). After t_1, $P = 375$ kW $< P_{\text{c1}}$, and the system is stable; after t_2, $P = 450$ kW $< P_{\text{c1}}$, and the system remains stable.

D. Case B

In status (IV), dc-bus capacitance is set to $C_m = 1$ mF that meets case B. Stability of dc microgrid must satisfy $P < P_{cm}$ $= 0.82$, the critical power P_{cm} is about 104.7 kW. After t_0, the power of CPL is 45 kW, $P < P_{cm}$ and the system is stable. After t_1, the power of CPL jumps up $P = 118$ kW $> P_{cm}$. HB occurs, and the dc-bus voltage has a periodic oscillation, as shown in Fig. 16(d).

When the parameters change according to status (V)–(VIII), P_{cm} increases. The dc-bus voltage waveforms are shown in Fig. 16 (f)–(h). No matter after t_0 or t_1, $P < P_{cm}$, and the dc-bus voltage remains stable. When $k_1 = 0.4$ and the parameters change according to status (IX). After t_1, $P = 118$ kW $> P_{cm}$, and HB occurs, as shown in Fig. 16(i).

In the above experiments, R_{L} and L_{L} are zero in Fig. 15(a), and the following will verify the assumption of the impedance in (4) and (5). According to status (IV), add $R_L = 0.06\ \Omega$, $L_L = 0.02$ mH, then recalculate the impedance of each branch and the new $G_{cm} = 1.19$ and $P_{cm} = 126.8$ kW. As can be seen from the right figure of Fig. 17, the output current of each DCS is basically distributed and changed according to (3). At t_1, when the power of CPL increases to 118 kW that is still less than the new P_{cm}, the system will remain stable, as shown in the left figure of Fig. 17. It is consistent with the theoretical analysis and verifies the correctness of the assumption.

VI. CONCLUSION

In this article, through the analysis of the symbols of the real parts of the eigenvalues, combined with the analysis of the static characteristics, the critical judgment conditions and parameter influence of the stability of the dc microgrid are obtained. The instability phenomenon of the system is analyzed by the bifurcation theory. The conclusions are as follows.

1) When the dc-bus capacitance C_m satisfies case A in Table II, reducing droop coefficient k of a DCS or increasing resistive R will improve the stable region that is $G < G_{c1}$. In case A, SNB mainly occurs.
2) When the dc-bus capacitance C_m satisfies case B Table II, increasing C_m, reducing resistive R and reducing the inductance of the DCS branch with the minimum ratio R_{di}/L_{di} will improve the stable region that is $G < G_{cm}$; increasing the droop coefficient of the DCS with the minimum ratio R_{di}/L_{di}, the stable region increases first and remains almost unchanged after reaching a certain value. In case B, HB may occur.
3) The stability of dc microgrid can be determined by the stability of the system at the lower boundary voltage on droop curves. The proposed stability judgment guidance of the system with only a few inequalities provide a simple method for stability judgment and design of dc microgrid.

Finally, the HIL experiment verifies the validity of the conclusions.

APPENDIX A
DERIVATION OF EQUATION (11)

From (10), we can obtain (28)

$$\frac{\prod_{i=1}^{n}\left(\lambda+\frac{R_{di}}{L_{di}}\right)}{C_m}\left(\sum_{j=1}^{n}\frac{1}{\lambda L_{dj}+R_{dj}}+\lambda C_m+\frac{1}{R}-\frac{P}{U_{\text{bus}}^2}\right)=0. \tag{28}$$

Set $\lambda = \sigma + j\omega$ and $G = P/U^2{}_{\text{bus}}$, and substitute them into (28)

$$\sum_{j=1}^{n}\frac{1}{(\sigma+j\omega)L_{dj}+R_{dj}}+(\sigma+j\omega)C_m+\frac{1}{R}-G=0. \tag{29}$$

According to (29), the real part and the imaginary part are separated

$$\begin{cases} G=\sum_{j=1}^{n}\frac{\sigma+R_{dj}/L_{dj}}{L_{dj}\left[(\sigma+R_{dj}/L_{dj})^2+\omega^2\right]}+\sigma C_m+\frac{1}{R} \\ 0=\sum_{j=1}^{n}\frac{-\omega}{L_{dj}\left[(\sigma+R_{dj}/L_{dj})^2+\omega^2\right]}+\omega C_m. \end{cases} \tag{30}$$

APPENDIX B
DERIVATION PROCESS OF THREE SITUATIONS UNDER CONDITION I

When $\sigma = 0$, G_{c1} is calculated from (14)

$$G_{c1}=\sum_{j=1}^{n}\frac{1}{R_{dj}}+\frac{1}{R}. \tag{31}$$

As shown in Fig. 9, the slope of the curve to the right of the dotted line $\sigma = \sigma_1$ is obtained from (14)

$$\frac{\mathrm{d}G_1}{\mathrm{d}\sigma}=-\sum_{j=1}^{n}\frac{L_{dj}}{\left(L_{dj}\sigma+R_{dj}\right)^2}+C_m. \tag{32}$$

Let σ_0 is the real eigenvalue of the minimum point of the curve to the right of the dotted line $\sigma = \sigma_1$, the minimum value is calculated from (14)

$$G_{c1\_\text{ot}}=\sum_{j=1}^{n}\frac{1}{L_{dj}\sigma_0+R_{dj}}+\sigma_0 C_m+\frac{1}{R}<G_{c1}. \tag{33}$$

1) Situation (1) (see curve 1 in Fig. 9)

The slope of curve 1 at $\sigma = 0$ is greater than zero, so the total capacitance of the dc-bus capacitors C_m meets the following condition obtained from (32)

$$C_m>\sum_{j=1}^{n}L_{dj}/R_{dj}^2. \tag{34}$$

According to curve 1, when $G > G_{c1}$, there is a positive solution for real part σ. Therefore, G_{c1} is the critical point of situation (1).

1) Situation (2) (see curve 2 in Fig. 9)

The slope of curve 2 at $\sigma = 0$ is equal to zero, so the total capacitance of the dc-bus capacitors C_m meets the following condition obtained from (32)

$$C_m=\sum_{j=1}^{n}L_{dj}/R_{dj}^2. \tag{35}$$

According to curve 2, $G_{c1} = G_{c1\_\text{ot}}$. When $G > G_{c1}$, there is a positive solution for real part σ. Therefore, G_{c1} is also the critical point of situation (2).

1) Situation (3) (see curve 3 in Fig. 9)

The slope of curve 3 at $\sigma = 0$ is less than zero, that is, C_m meets the following condition obtained from (32):

$$C_m<\sum_{j=1}^{n}L_{dj}/R_{dj}^2. \tag{36}$$

According to curve 3, when $G > G_{c1\_\text{ot}}$, there is one or two positive solutions for real part σ. Therefore, G_{c1_ot} is the critical point of situation (3). But known from (33), G_{c1_ot} contains unknown quantity σ_0. (37) can be obtained after taking the derivative of (14)

$$\frac{\mathrm{d}G_1}{\mathrm{d}\sigma}\Big|_{\sigma=\sigma_0}=0\Rightarrow\sum_{j=1}^{n}\frac{L_{dj}}{\left(L_{dj}\sigma_0+R_{dj}\right)^2}=C_m,\sigma_0>0. \tag{37}$$

By substituting (37) into (33), G_{c1_ot} is further derived and reduce to G_{cm} that is calculable. As can be seen from Fig. 11, the gap between the two points is quite small. So G_{c1_ot} is substituted by G_{cm} as the critical point in this article

$$\begin{aligned} G_{c1\_\mathrm{ot}} &= \sum_{j=1}^{n} \frac{1}{L_{dj}\sigma_0+R_{dj}} + \sigma_0 C_m + \frac{1}{R} \\ &= \sigma_0 \sum_{j=1}^{n} \frac{L_{dj}}{(L_{dj}\sigma_0+R_{dj})^2} \\ &\quad + \sum_{j=1}^{n} \frac{L_{dj}}{(L_{dj}\sigma_0+R_{dj})^2}\cdot\frac{R_{dj}}{L_{dj}} + \sigma_0 C_m + \frac{1}{R} \\ &\geq 2\sigma_0 C_m + C_m\cdot \min_{j=1}^{n}(R_{dj}/L_{dj}) + \frac{1}{R} \\ &\geq C_m\cdot \min_{j=1}^{n}(R_{dj}/L_{dj}) + \frac{1}{R} = G_{cm}. \end{aligned} \tag{38}$$

REFERENCES

[1] X. Guo, Z. Lu, B. Wang, X. Sun, and J. M. Guerrero, “Dynamic phasors-based modeling and stability analysis of droop-controlled inverters for microgrid applications,” *IEEE Trans. Smart Grid.*, vol. 5, no. 6, pp. 2980–2987, Nov. 2014.

[2] X. Lu, K. Sun, J. M. Guerrero, J. C. Vasquez, L. Huang, and J. Wang, “Stability enhancement based on virtual impedance for DC microgrids with constant power loads,” *IEEE Trans. Smart Grid.*, vol. 6, no. 6, pp. 2770–2783, Nov. 2015.

[3] L. Meng, T. Dragicevic, J. Roldan-Perez, J. C. Vasquez, and J. M. Guerrero, “Modeling and sensitivity study of consensus algorithm-based distributed hierarchical control for DC microgrids,” *IEEE Trans. Smart Grid.*, vol. 7, no. 3, pp. 1504–1515, May 2016.

[4] Z. Zhao, P. Yang, Y. Wang, Z. Xu, and J. M. Guerrero, “Dynamic characteristics analysis and stabilization of PV-based multiple microgrid clusters,” *IEEE Trans. Smart Grid.*, vol. 10, no. 1, pp. 805–818, Jun. 2019.

[5] D. Chen, Y. Xu, and A. Q. Huang, “Integration of DC microgrids as virtual synchronous machines into the AC grid,” *IEEE Trans. Ind. Electron.*, vol. 64, no. 9, pp. 7455–7466, Sep. 2017.

[6] V. Nasirian, S. Moayedi, A. Davoudi, and F. L. Lewis, “Distributed cooperative control of DC microgrids,” *IEEE Trans. Power Electron.*, vol. 30, no. 4, pp. 2288–2303, Apr. 2015.

[7] J. M. Guerrero, M. Chandorkar, T. Lee, and P. C. Loh, “Advanced control architectures for intelligent microgrids—Part I: Decentralized and hierarchical control,” *IEEE Trans. Ind. Electron.*, vol. 60, no. 4, pp. 1254–1262, Apr. 2013.

[8] X. Lu, J. M. Guerrero, S. Kai, and J. C. Vasquez, “An improved droop control method for DC microgrids based on low bandwidth communication with DC bus voltage restoration and enhanced current sharing accuracy,” *IEEE Trans. Power Electron.*, vol. 29, no. 4, pp. 1800–1812, Apr. 2013.

[9] A. M. Rahimi and A. Emadi, “Active damping in DC/DC power electronic converters: A novel method to overcome the problems of constant power loads,” *IEEE Trans. Ind. Electron.*, vol. 56, no. 5,pp. 1428–1439, May 2009.

[10] L. Herrera, Z. Wei and W. Jin, “Stability analysis and controller design of DC microgrids with constant power loads,” *IEEE Trans. Smart Grid.*, vol. 8, no. 2, pp. 881–888, Mar. 2017.

[11] X. Chang, Y. Li, L. Xuan, and X. Chen, “An active damping method based on a supercapacitor energy storage system to overcome the destabilizing effect of instantaneous constant power loads in DC microgrids,” *IEEE Trans. Energy Conver.*, vol. 32, no. 1, pp. 36–47, Mar. 2017.

[12] R. D. Middlebrook and S. Cuk, “A general unified approach to modelling switching-converter power stages,” *in Proc. IEEE Power Electron. Spec. Conf.*, 1976, pp. 18–34.

[13] S. Cuk and R. D. Middlebrook, “A general unified approach to modeling switching DC-DC converters in discontinuous conduction mode,” in *Proc. IEEE Power Electron. Spec. Conf.*, 1977, pp. 36–57.

[14] R. D. Middlebrook and S. Cuk, “Input filter considerations in design and application of switching regulators,” in *Proc. IEEE Ind. Appl. Soc. Annu. Meeting*, 1976, pp. 366–382.

[15] J. Yang, Z. Hui and Z. Na, “Small-signal stability analysis of islanded DC microgrid under DBS control,” in *Proc. IEEE 8th Int. Power Electron. Motion Control Conf.*, Hefei, China, 2016, pp. 1770–1775.

[16] S. Liu, W. Zhu, Y. Cheng, and B. Xing, “Modeling and small-signal stability analysis of an islanded DC microgrid with dynamic loads,” in *Proc.15th IEEE Int. Conf. Environ. Elect. Eng.*, Rome, Italy, Jun. 2015, pp. 866–871.

[17] J. Chen and J. Chen, “Stability analysis and parameters optimization of islanded microgrid with both ideal and dynamic constant power loads,” *IEEE Trans. Ind. Electron.*, vol. 65, no. 4, pp. 3263–3274, Apr. 2018.

[18] V. Mariani, F. Vasca, J. C. Vasquez, and J. M. Guerrero, “Model order reductions for stability analysis of islanded microgrids with droop control,” *IEEE Trans. Ind. Electron.*, vol. 62, no. 7, pp. 4344–4354, Jul. 2015.

[19] A. P. N. Tahim, D. J. Pagano, E. Lenz, and V. Stramosk, “Modeling and stability analysis of islanded dc microgrids under droop control,” *IEEE Trans. Power Electron.*, vol. 30, no. 8, pp. 4597–4607, Aug. 2015.

[20] Q. Xu*et al.*, “A decentralized dynamic power sharing strategy for hybrid energy storage system in autonomous DC microgrid,” *IEEE Trans. Ind. Electron.*, vol. 64, no. 7, pp. 5930–5941, Jul. 2017.

[21] S. Vesti, T. Suntio, J. A. Oliver, R. Prieto, and J. A. Cobos, “Impedance-Based stability and transient-performance assessment applying maximum peak criteria,” *IEEE Trans. Power Electron.*, vol. 28, no. 5, pp. 2099–2104, Jul. 2013.

[22] X. Feng, Z. Ye, K. Xing, F. C. Lee, and D. Borojevic, “Individual load impedance specification for a stable DC distributed power system,” in *Proc.14th Annu. Appl. Power Electron. Conf. Expo.*, Mar. 1999, pp. 923–929.

[23] S. D. Sudhoff, S. F. Glover, P. T. Lamm, D. H. Schmucker, and D. E. Delisle, “Admittance space stability analysis of power electronic systems,” *IEEE Trans. Aerosp. Electron. Syst.*, vol. 36, no. 3, pp. 965–973, Jul. 2002.

[24] S. D. Sudhoff and J. M. Crider, “Advancements in generalized immittance based stability analysis of DC power electronics based distribution systems,” in *Proc. IEEE Elect. Ship Technol. Symp.*, 2011, pp. 207–212.

[25] S. Anand and B. G. Fernandes, “Reduced-order model and stability analysis of low-voltage DC microgrid,” *IEEE Trans. Ind. Electron.*, vol. 60, no. 11, pp. 5040–5049, Nov. 2013.

[26] X. Chen, M. Shi, H. Sun, Y. Li, and H. He, “Distributed cooperative control and stability analysis of multiple DC electric springs in a DC microgrid,” *IEEE Trans. Ind. Electron.*, vol. 65, no. 7, pp. 5611–5622, Jul. 2018.

[27] Z. Shuai, Y. Hu, Y. Peng, C. Tu, and Z. J. Shen, “Dynamic stability analysis of synchronverter-dominated microgrid based on bifurcation theory,” *IEEE Trans. Ind. Electron.*, vol. 64, no. 9, pp. 7467–7477, Sep. 2017.

[28] E. Lenz, D. Pagano and A. Tahim, “Codimension-Two bifurcation analysis in DC microgrids under droop control,” *Int. J. Bifurcat. Chaos*, vol. 26, 2016, Art. no. 1650028.

Haiyuan Liu received the B. S. degree from Sichuan Normal University, Chengdu, China, in 2001, and the M.S. and Ph.D. degrees from the China University of Mining and Technology, Xuzhou, China, in 2006 and 2019, respectively.

She is currently a Teacher with the School of Mathematics, China University of Mining and Technology, Xuzhou, China. Her current research interests include intelligent control theory and its application.

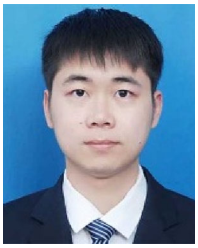

Wenzhong Guo was born in 1996. He received the B.S. degree in electrical engineering from the Hefei University of Technology, Hefei, China, in 2019. He is currently working toward the M.S. degree in power electronics with the China University of Mining and Technology, Xuzhou, China.

His current research interests include dc microgrids, photovoltaic inverters, and HVdc grids.

Dong Cheng received the B.S. degree from Tianjin University, Tianjin, China, in 1987, the M.S. degree from then Xi’an University of Technology, Xi’an, China, in 1990, and the Ph.D. degree from Northwestern Polytechnical University, Xi’an, China, in 2011.

He is currently a Professor-Level Research Fellow in the CSIC 713th Research Institute. His research interests include electromechanical engineering design and control.

Yingjie Wang (Member, IEEE) received the B.E. degree in mechanical engineering from Central South University, Changsha, China, in 2001, and the Ph.D. degree in electrical engineering from the China University of Mining and Technology, Xuzhou, China, in 2012.

He is currently an Assistant Professor with the School of Information and Electrical Engineering, China University of Mining and Technology, where he is currently working in the areas of power quality, microgrid, and medium-voltage ac drives.

Min Wang received the B. S. degree in electrical engineering from the Jiangxi University of Science and Technology, Ganzhou, China, in 2017. He is currently working toward the M. S. degree in electrical engineering with the China University of Mining and Technology, Xuzhou, China.

His current research interests include power quality and microgrids.